Liquid Crystal Uncooled Thermal Imager Development

September 9, 2014

H.R. Clark Jr., C.O. Bozler, S.R. Berry and R.K. Reich[1]
MIT Lincoln Laboratory
244 Wood Street
Lexington, MA 02420-9108

P.J. Bos, V.A. Finnemeyer and D.R. Bryant
Kent State University Liquid Crystal Institute
1425 University Esplanade
Kent, OH 44242-0001

ABSTRACT

An uncooled thermal imager is being developed based on a liquid crystal transducer. The liquid crystal transducer changes a long-wavelength infrared scene into a visible image as opposed to an electric signal in microbolometers. This approach has the potential for making a more flexible thermal sensor. One objective is to develop imager technology scalable to large formats (tens of megapixels) while maintaining or improving the noise equivalent temperature difference (NETD) compared to microbolometers. Our work is demonstrating that the liquid crystals have the required performance (sensitivity, dynamic range, speed, etc.) to make state-of-the-art uncooled imagers. A process has been developed and arrays have been fabricated using the liquid crystals. A breadboard camera system has been assembled to test the imagers. Results of the measurements are discussed.

Keywords: thermal imager, liquid crystals, uncooled imagers, long-wavelength infrared, microbolometers, optical readout.

Session Designation: Meeting Session A: Uncooled IR Detector and FPA Technology Paper/Presentation (DA06)

This work was sponsored by the Assistant Secretary of Defense (ASD) for Research and Engineering (R&E) under Air Force Contract No. FA8721-05-C-0002. Opinions, interpretations, conclusions, and recommendations are those of the authors, and do not necessarily represent the view of the United States Government.

1.0 Introduction

Uncooled thermal detectors have become an indispensable sensor technology in military long-wavelength infrared (LWIR) imaging applications. The devices have progressed to where the sensitivity and resolution are sufficient to replace cooled detectors in many applications [1, 2]. However, the state-of-the-art uncooled sensor technology, namely microbolometers based on thermistors, has progressed slowly over the past few years. Some of the challenges with these arrays include: difficulties in scaling to larger formats, increasing noise with decreasing pixel size, and high fabrication cost.

This paper describes an imager concept with an optical readout that separates the IR-to-optical conversion process [3-5] from the electronic readout. The decoupling simplifies the sensor architecture and enables independent optimization of components. The detector uses sensitive liquid crystals (LCs) to detect small changes in temperature created by an infrared image and uses remote detection of polarized visible light by a solid-state imager to change the signal into a usable digital electronic output. A charge-coupled device (CCD) or CMOS active pixel sensor (APS) could be used as the visible light imager.

2.0 Sensor Concept

Figure 1 shows the sensor concept for the thermal imager where the CMOS readout integrated circuit (ROIC) is separated from the LC thermal transducer.

The sensor operation is briefly described as follows:

- An IR image is focused on the thermally resistive pedestal array containing the LCs (transducer)
- The LCs experience a temperature change
- This temperature change induces a change in the LC's birefringence
- The change in birefringence is sensed by polarized visible light passing through the LC (IR-to-visible conversion completed)
- The visible light passes through a second polarizer and is focused onto a CCD or CMOS APS imager
- Electronic video is readout from the solid state imager.

The relatively large change in birefringence with temperature [6] results in a measurable variation in intensity. Note it is the polarized light that is creating an intensity change in the electronic image from the solid-state detector. Thus, the sensor system converts the LWIR light into an electronic image.

The new type of thermal imager would leverage the ever expanding display and visible solid-state imager technology that has become low cost and has high resolution. Visible sensors have been rapidly increasing in pixel counts and also increasing in dynamic range (e.g. charge capacity or bits per unit area) that enables the approach discussed.

2.1 Decoupling and Component Optimization

In this imager the electronic readout is remote from the IR-to-visible converter (transducer). This simplifies the detector and enables the optimization of the individual components. In contrast, microbolometers have the CMOS ROIC monolithically integrated with the microbolometers. Also, the support legs of the microbolometer structure have to be both thermally insulating and electrically conductive, which limits achievable thermal resistance. These constraints negatively impacts material selection, pixel size, fabrication complexity, yield, and performance.

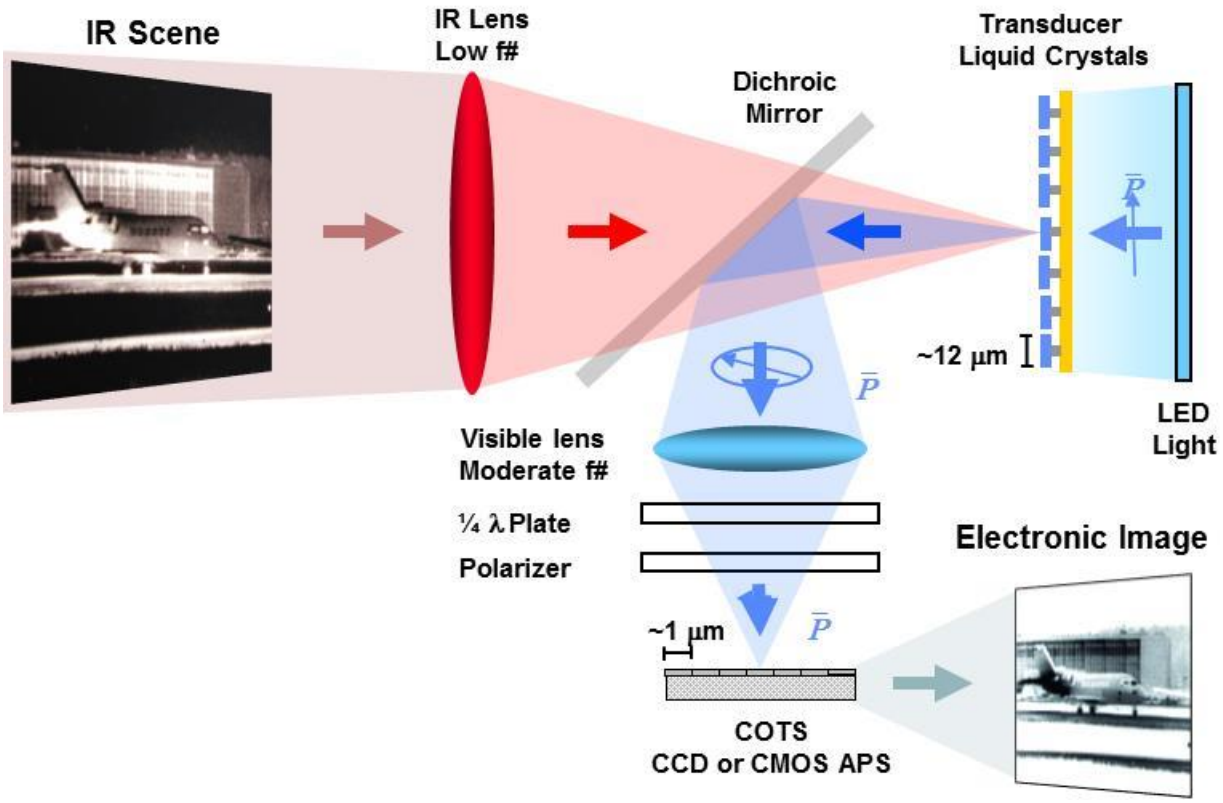

Figure 1. Thermal imager concept based on temperature sensitive LCs.

2.2 IR-to-Visible Transducer Structure

The IR-to-visible conversion is done by a transducer that has pixels that consist of a thermally insulated pedestal with LCs and IR absorber layers on top. The structure labeled "Transducer Liquid Crystals" in Figure 1 schematically shows this structure. The elevated cavity structure with LCs inside has not been built before, and a new process technology needs to be developed. The pedestal structure provides mechanical support for the LC, thermal isolation from adjacent pixels and thermal resistance to the transparent substrate. The LC and pedestal are cooperatively designed for sensitivity and fast millisecond response times.

2.3 Liquid Crystals

The basis of the thermal imager concept considered is to optically measure the thermally induced change in the molecular order, quantified by the LC order parameter "S" [6]. In LCs, changes in the molecular thermal order parameter can affect material optical birefringence that can be measured using a remote detection technique.

2.4 Remote Visible Sensor

The remote visible sensor, labeled "CCD or CMOS APS" in Figure 1, converts the visible light that has passed through the LC to an electronic image. Since S is a molecular parameter, any change in the temperature of the LC will induce a change in birefringence with a response time on the order of that for molecular fluctuations (<1 microsecond). This change in birefringence will cause a change in intensity of the visible light incident on the CCD or CMOS sensor. The sensor will produce still or video images.

3.0 Liquid Crystals

3.1 Material

The thermal-optical properties of LCs have been investigated previously by, among others, the Army Night Vision Laboratory and Kent State in the 1970s and early 1980s [3-5]. Researchers demonstrated that the birefringence of the LCs could be used to detect small changes in temperature.

To understand the imager operation some background in LCs is needed. They are a state of matter that is distinct from the usual solid, liquid, and gas states [3]. Figure 2 illustrates the different states for solid crystals, LCs, and isotropic liquids. If the molecules of a material are highly elongated, as in having a pencil shape as shown in Figure 2, two types of order can be formed when passing from the normal liquid state to the solid state. One is that the elongated molecular axis is aligned, and the other is that the molecule's center of mass lay on a grid.

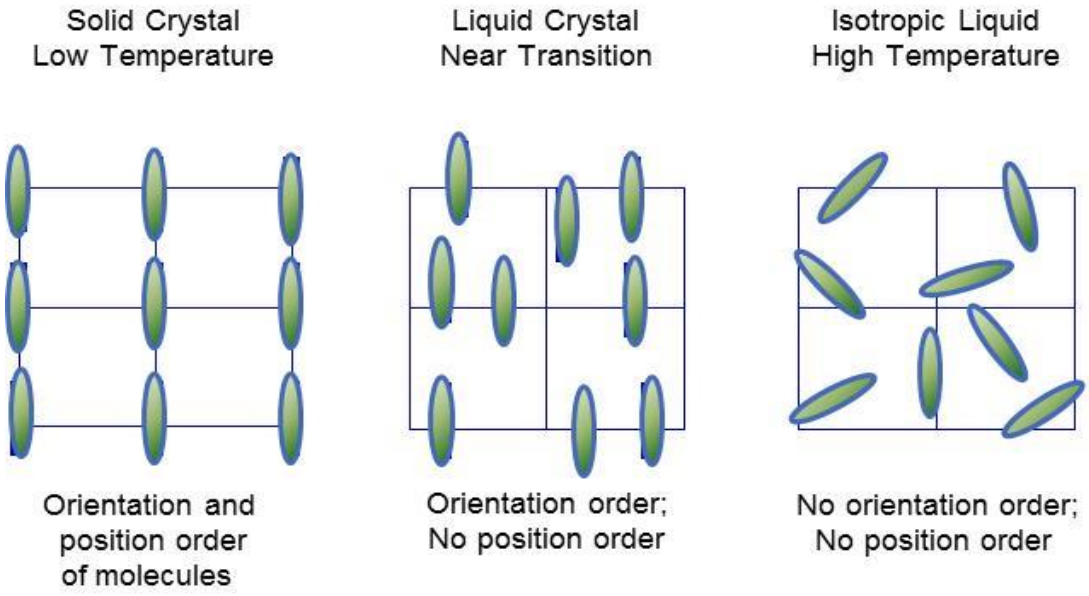

Figure 2. States of matter for solid crystals, LCs, and liquids.

Figure 3 is an illustration of a nematic LC molecule showing the indices of refraction. The indices of refraction are related to the thermally averaged LC molecule, whose orientation is depicted. The nematic LC has the extraordinary index of refraction n_e for light polarized along the long axis of the averaged

molecular orientation and the ordinary index of refraction n_o along the other two orthogonal directions. The birefringence is the difference between the two indices, $\Delta n = n_e - n_o$. For the LC state of matter (in this case nematic), the elongated axis of the molecule has a tendency to be aligned, but the center of mass of

the molecules is free to move about as a liquid. Unlike a solid, the ordering of the long molecular axis is not perfect. The principal axis of the molecules thermally fluctuates about an average direction called the "director". The degree of order of the thermally fluctuating molecules is quantified by the quantity $S = \langle 3/2 \cos^2 \theta - 1/2 \rangle$ where θ is the angle of the molecular axis with respect to the director axis.

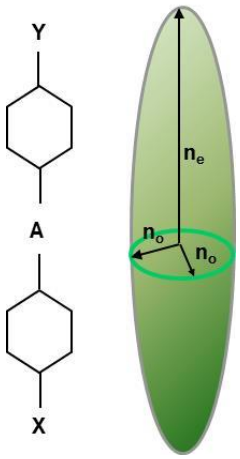

Figure 3: Liquid crystal molecule showing indices of refraction n_e, n_o.

The birefringence, Δn, *is proportional to the* order parameter S and has been shown from mean-field calculations [6] to have temperature dependence of that given in Figure 4. The interest in an LC as an optical detector is in its relatively high birefringence Δn where it can be greater than 0.2.

For the thermal imager arrays being developed, we rely on the change in the S with temperature to change the birefringence, (unlike display manufacturers that prefer no change in S with temperature). The two different indices of refraction cause the electromagnetic fields to travel as two modes with different velocities. This results in a phase change between the two electromagnetic modes and a change in the polarization state. This effect can be used to change the light transmission of the device between polarizers. Therefore: a change in temperature causes a change in the birefringence (difference in the indices of refraction) and thus in the polarization state and subsequent intensity of light transmitted through an analyzer.

This effect is different from the electrooptical effect in display devices where the "effective" birefringence is varied by changing the angle between the light propagation direction and the averaged molecular orientation. In the case of this device, the change in birefringence with temperature is related to a change in the molecular level order, and the temperature sensing is not related to changes in bulk properties of viscosity or elasticity.

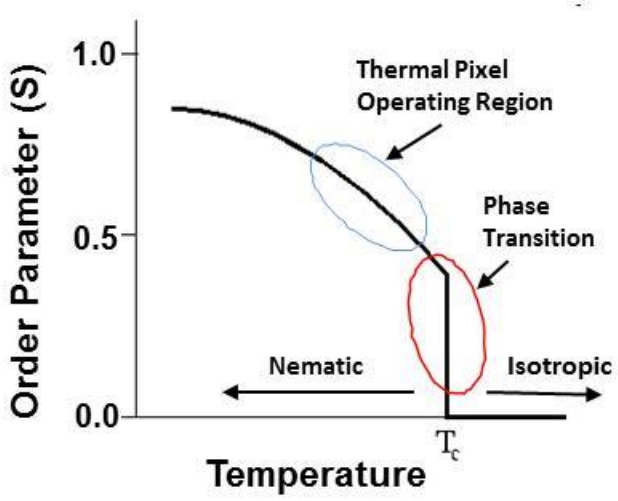

Figure 4. Order parameter (S) versus temperature.

4.0 Liquid Crystal Transducer Design and Fabrication

4.1 Design

The details of the LC transducer concept are shown in Figure 5. The transducer consists of a LC cavity that is 20 µm × 20 µm × 1 µm, which is elevated off a transparent substrate approximately 1 to 2 µm by four nitride legs (2 µm wide × 300 nm thick). The nitride legs provide the thermal insulation for the transducer. The top surface of the cavity is also a 300-nm-thick nitride layer. In most of the pixels developed, four legs are used instead of two for mechanical stability of the prototype pixel structures.

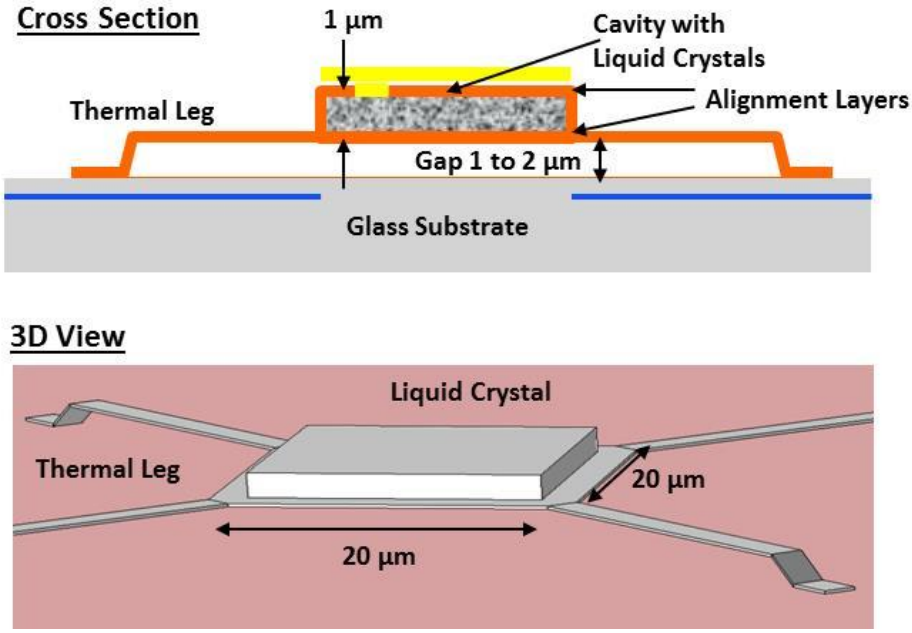

Figure 5. Liquid crystal transducer design.

4.2 Alignment

To be useful for sensitive temperature measurements in the system described in Section 3, the LCs must have a determined alignment. This requires an alignment layer that seeds the orientation of the LC molecules. Figure 6 depicts a LC cell showing the location of the alignment layers. The alignment layer has an anchoring energy which determines how much energy is required to change the orientation of the surface contacting director. The alignment fluctuation noise is related to the anchoring energy; the higher the energy the lower the thermal director fluctuation (less noise).

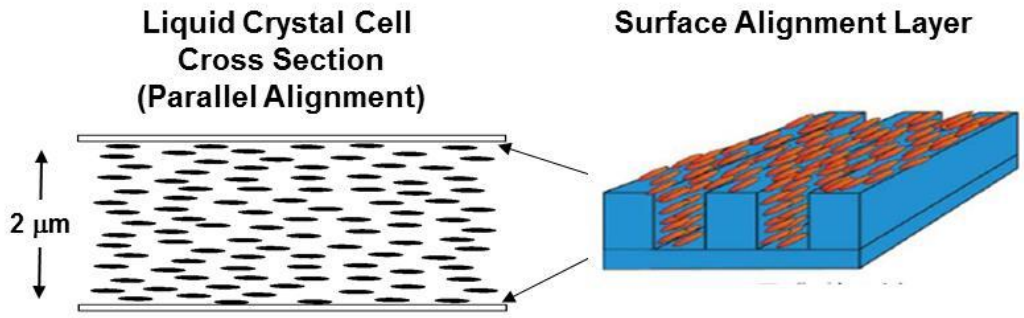

Figure 6. Liquid crystal cell with planar alignment showing location of alignment surface.

Several alignment methods have been considered such as rubbed polyimide [7], ionic milling [8], lapped inorganics [9], glancing angle deposition [10], and photo-alignment [11]. Most displays use polyimide alignment layers [7] that are coated and mechanically rubbed to elongate the polymer chains to create an anisotropic van der Waals interaction that aligns the LC director with a large anchoring energy. In practice, the polyimide is deposited on two relatively large flat glass pieces and then the pieces are brought together within a few microns, the gap being set by glass ball spacers. In the thermal imager application where isolated cavities with lateral dimensions of microns are desired, unfortunately some of the polyimide properties are not compatible. Therefore, the alignment technique is done by mechanical diamond lapping of surfaces (e.g. silicon dioxide, molybdenum). The lapping creates parallel “troughs” with dimension of several nanometers in height and width. Also, the top and bottom alignment layers are parallel for the bulk cells and devices that have been fabricated. Other alignment techniques are also being investigated that will be more VLSI-compatible such as photoalignment.

4.3 Processing

Figure 7 illustrates the major steps in the process flow used to fabricate the thermal pixel imager on fused silica or silicon substrates. The first arrays fabricated are proof of concept devices where some of the constraints, such as fill factor, are relaxed to ease fabrication. The LC transducer is intended to operate in transmission. However, the pathfinder arrays are fabricated on silicon substrates and thus are characterized in the reflection mode. The fabrication process has fewer than 10 photolithographic steps to create the transducer. This should be compared to greater than 40 mask steps for a conventional microbolometer.

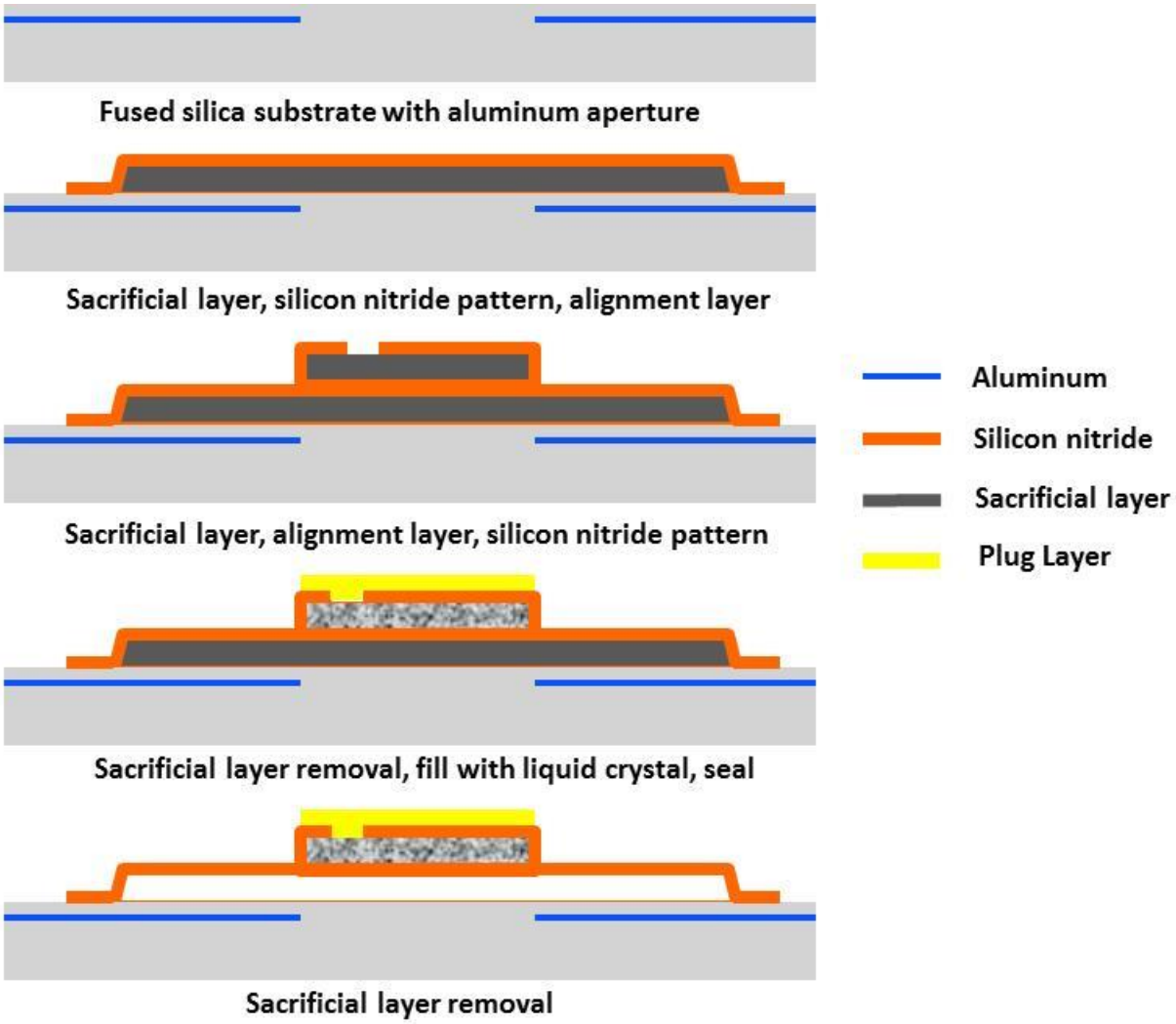

Figure 7. Major process steps in fabricating the LC thermal imager.

The mask set has arrays as large as 256 × 256 pixels with four thermal legs. Several smaller arrays that are also on the mask set have various structures including thermal pixels with two thermal legs. Various test structures are also fabricated with the LC transducer devices for characterization of the pixel structure's optical, mechanical, thermal, and temporal properties as well as process control monitors.

Processing begins on bare 200-mm fused silica wafers. An aluminum blocking layer is deposited and windows are opened. The light is blocked everywhere except where it will pass through the LC. A silicon dioxide layer is deposited and a planarizing polish is done. A 1- to 2-µm-thick molybdenum sacrificial layer is deposited on top of the oxide and dry etched. Next, a 300-nm-thick silicon nitride layer is deposited and dry etched to form the thermal legs and the bottom of the LC cavity. A silicon dioxide layer, 100 nm thick, is deposited and diamond lapped to generate an alignment surface. A second 1-µm-thick molybdenum sacrificial layer is deposited and etched to define the cavity interior. A second diamond lapping is done to create the top alignment layer in the cavity. A 300-nm-thick silicon nitride layer is deposited again and dry etched to form the top surface and sides of the cavity. During this etch, a 2-µm-diameter hole for filling the cavity with LCs is also created in the silicon nitride on top of the

cavity. After the hole is formed, the top molybdenum sacrificial layer is etched in hydrogen peroxide. The bottom molybdenum is protected during this step by the 100-nm-thick silicon dioxide layer and photoresist. Once the molybdenum is removed from the cavities, LCs are then poured over the cavity surface. The LCs easily wet the silicon nitride surface and are spontaneously wicked through the 2-µm-diameter hole into the cavity. The LC used in most of the experiments is 4′-pentyl-4-biphenylcarbonitrile **(**5CB) although other LC mixtures have worked equally well.

The bulk LC is then rinsed off the surface with deionized water. The amorphous fluoropolymer CYTOP (Asahi Glass Co.) is spun over the thermal imager devices and annealed to plug the cavities. The CYTOP is then patterned and etched in an oxygen-plasma to open holes over the bottom molybdenum. Using CYTOP as a mask, the protective oxide layer is etched with buffered hydrofluoric acid, exposing the bottom molybdenum. Once the silicon dioxide is removed from the holes, a second pattern and etch is done to the CYTOP, which forms the cavity plug. The bottom molybdenum is then removed using hydrogen peroxide. The silicon dioxide layer over the bottom molybdenum acts as a support keeping the cavities elevated during the wet hydrogen peroxide etch process. The final process step removes the silicon dioxide layer through an ion milling process that releases the filled cavities.

Figure 8 shows an illustration of the cross-section of finished devices, an optical microscope photograph of a pixel and arrays filled with LCs, and scanning electron micrographs (SEMs) of the pixel arrays.

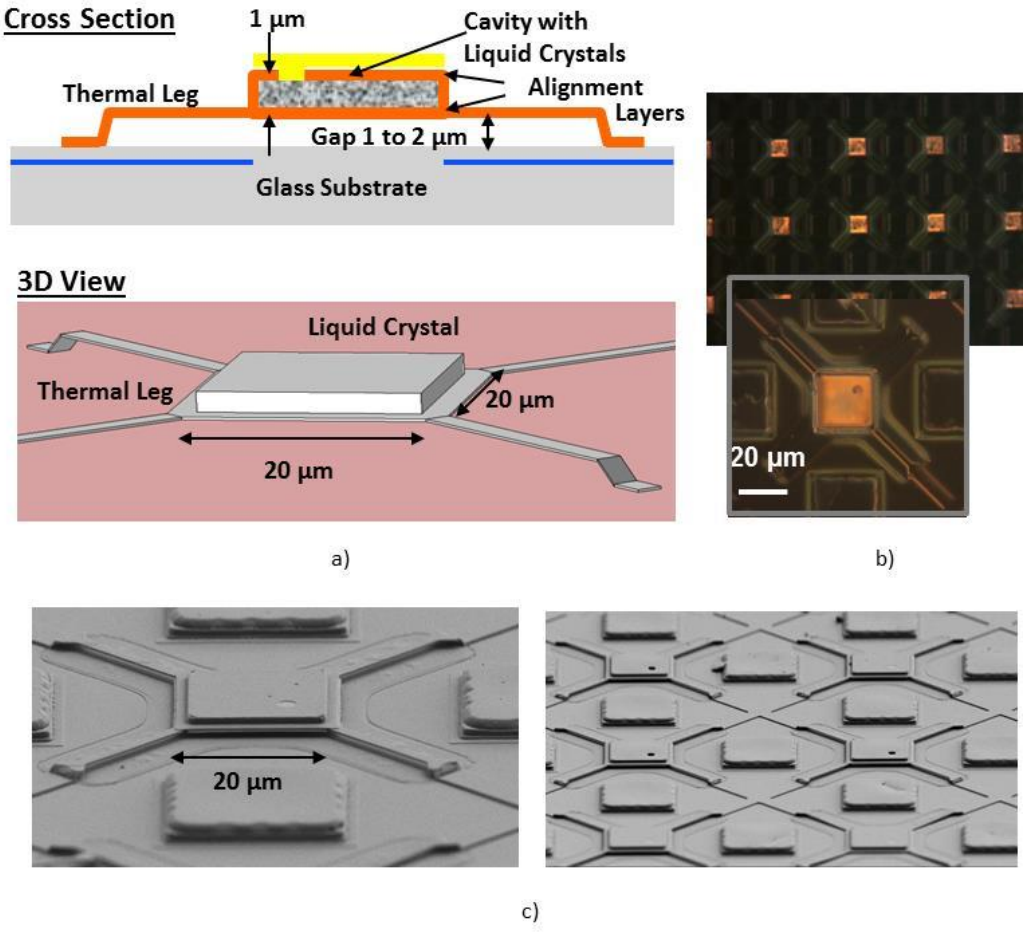

Figure 8. a) Illustration of pixel cross-section and corresponding 3D view, b) LC-filled cavity viewed with polarized light, and c) SEM photograph of a thermal pixel and arrays.

The first arrays fabricated have low fill factors where the emphasis has been on proof of concept of the LC thermal imager and establishing a process instead of optimizing performance.

5.0 Measurements

Measurements are done on LC cells, both larger-area sample cells and small cells of device arrays. The bulk cells are relatively simple to fabricate and give preliminary performance information for feasibility of the imager concept. The measurements are done at 2 K to 3 K from the phase transition except where noted. The LC used in the measurements is 5CB because the phase transition is conveniently located at 308 K although other LC mixtures tested showed similar performance.

5.1 Large Area Cell Measurements

Figure 9 is a photograph of 1-inch cells that are used in the characterization experiments. The cells consist of two glass slides with one side of each slide having indium tin oxide (ITO) covered by an alignment layer (e.g. rubbed polyimide or lapped silicon dioxide). The ITO is a standard in these cells for evaluating switching display processes, but the electrical switching is not used or needed in our measurements or operation of the thermal imager. A 2- to 3-µm-thick LC layer is injected between the glass slides with the LC facing the alignment layers. The thickness of the LC is part of the imager design and is chosen to give a response time of 10 ms based on reasonable thermal resistance values expected for silicon nitride legs used in the arrays.

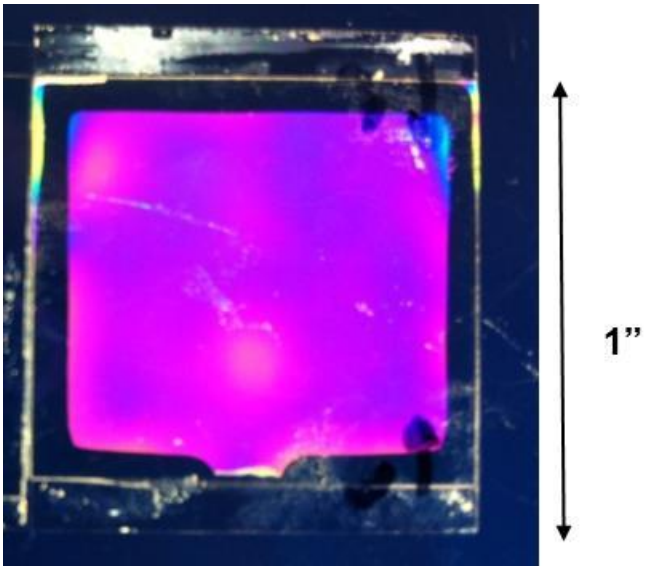

Figure 9. Liquid crystal cells used in experiments.

Figure 10 is a schematic of the system used in the testing. The arrangement of the optical axes of the elements is that for a Senarmont measurement system [12]. For this measurement technique the output polarization state will always be linear after the quarter wave plate and results in the maximum signal through the analyzer for a single-point measurement.

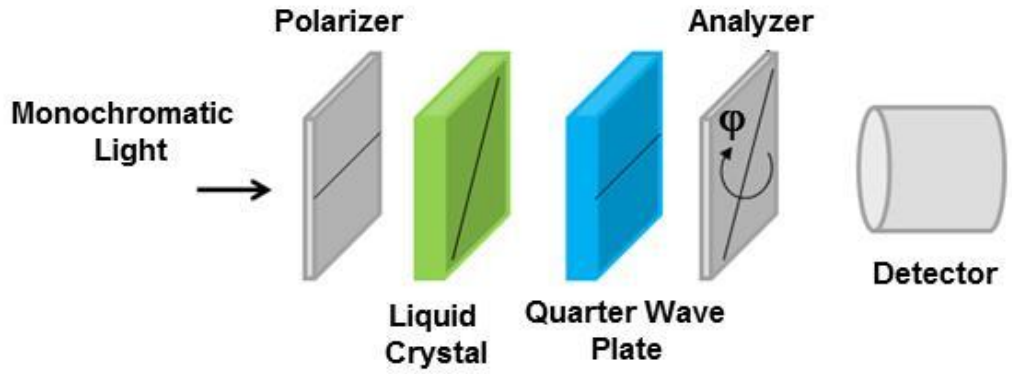

Figure 10. Senarmont system cartoon showing the location and orientation of optical components.

The Senarmont signal is given by the equation

$$I = I_o cos^2(\varphi + \frac{\Gamma}{2}) \tag{1}$$

where I is the signal intensity at the detector, I_o is the input intensity, φ is the analyzer angle, and Γ is the retardation. The retardation is

$$\Gamma = \frac{2\pi\, \Delta n(T) d}{\lambda} \tag{2}$$

where $\Delta n(T)$ is the temperature dependent birefringence, d is the thickness of the LC layer, and λ is the visible wavelength of the input light (the quarter wave plate is optimized for λ). The Senarmont optical arrangement allows for the value of φ to be adjusted to give the maximum change in intensity with temperature for a given value of Γ (that is dependent on the cavity thickness).

Figure 11 plots the Senarmont signal, signal standard deviation and signal to noise (SNR) versus analyzer angle. The SNR is defined as $\Delta I / (\sqrt{2}\ \sigma_I)$, where ΔI is the change in signal for a degree change in the analyzer angle and σ_I is the signal intensity standard deviation. The $\sqrt{2}$ term in the equation takes into account the subtraction of two signals.

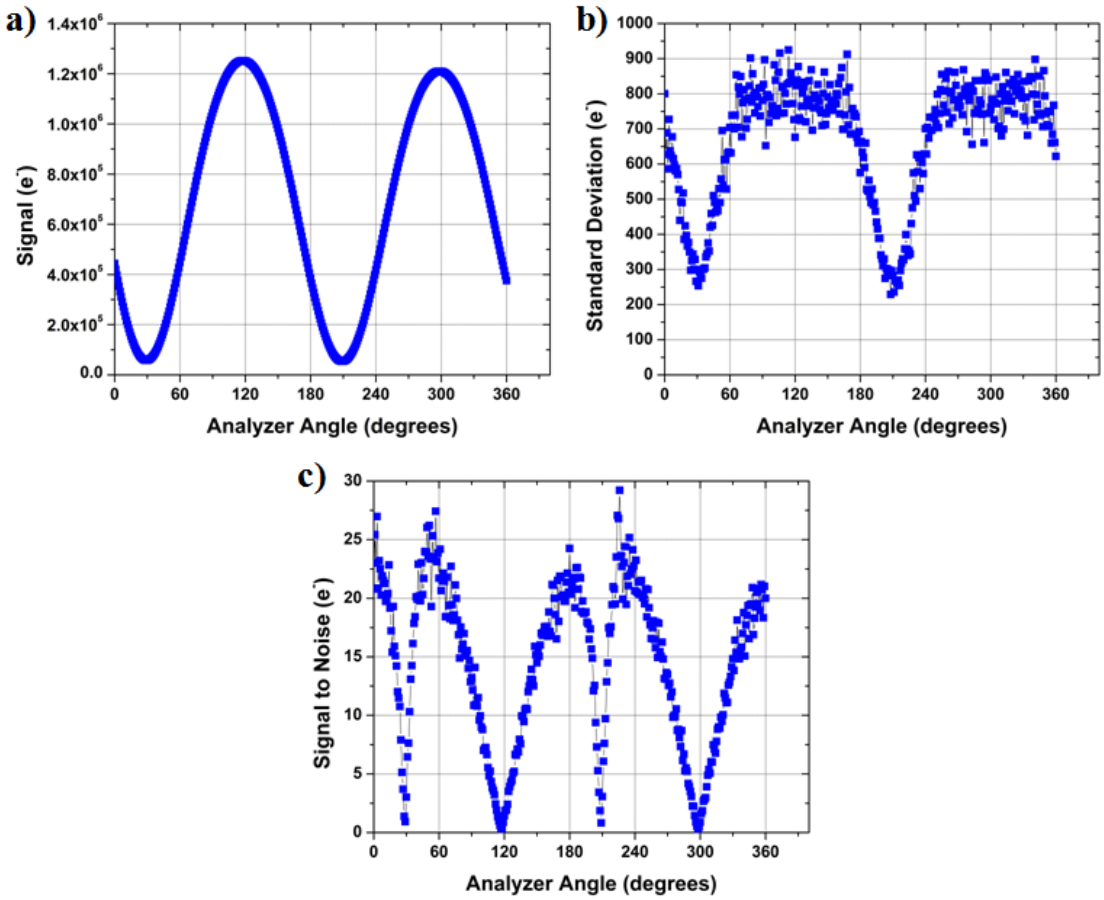

Figure 11. Plots of a) Senarmont signal, b) standard deviation, and c) signal-to-noise per analyzer degree.

The noise (standard deviation) for most of the measurements is limited by the Poisson distribution of the input light signal. When this condition is true, higher input signals result in higher SNR. Fluctuations from the LCs are observed at high-input-light signal levels beyond where the thermal imager is expected to operate and thus do not affect the SNR. The fluctuations observed at these high-light levels are caused by the twist, bend, and splay motions of the LCs.

The maximum SNR is at an analyzer setting of about 25° to 35° from the signal minimum with the location depending on the noise. In the temperature sensitivity measurements, the analyzer is set at approximately the peak SNR, which should be near the maximum change in intensity with temperature. The measurements start at an analyzer setting such that the SNR peak occurs in the middle of a temperature scan. Note the signal has been increased to improve the peak SNR. This causes some distortion in the higher signal levels in the Senarmont curve, but it is far away from the peak SNR.

Figure 12 shows the temperature sensitivity of the LC cells. The LC cells are placed on a substrate with a heater driven by a controller capable of 2-mK steps. The assembly is then placed in a dewar that is evacuated to below 1 mTorr. The visible-image detector is a 640×480 CCD camera operating at 30 Hz or 60 Hz. A 24-µm area of the LC is imaged onto a 4×4 pixel area of the imager. The pixels are binned to increase the detected photoelectrons from the light passing through the LC area. The change in signal with temperature is measured by a change in intensity with the analyzer held constant.

The data in Figure 12 give the change in intensity, in digital numbers, for 2 mK temperature steps. Approximately 100 frames are taken at each step with the camera operating at the 30 Hz or 60 Hz rate. The standard deviation calculated from a 2 mK step is about 225 µK. This can be related to a noise equivalent temperature difference (NETD) in the scene of about 18 mK by making the usual assumptions [13] (e.g. 24-µm pixel, 30 Hz frame rate, f/1 lens, typical leg thermal resistance, etc.).

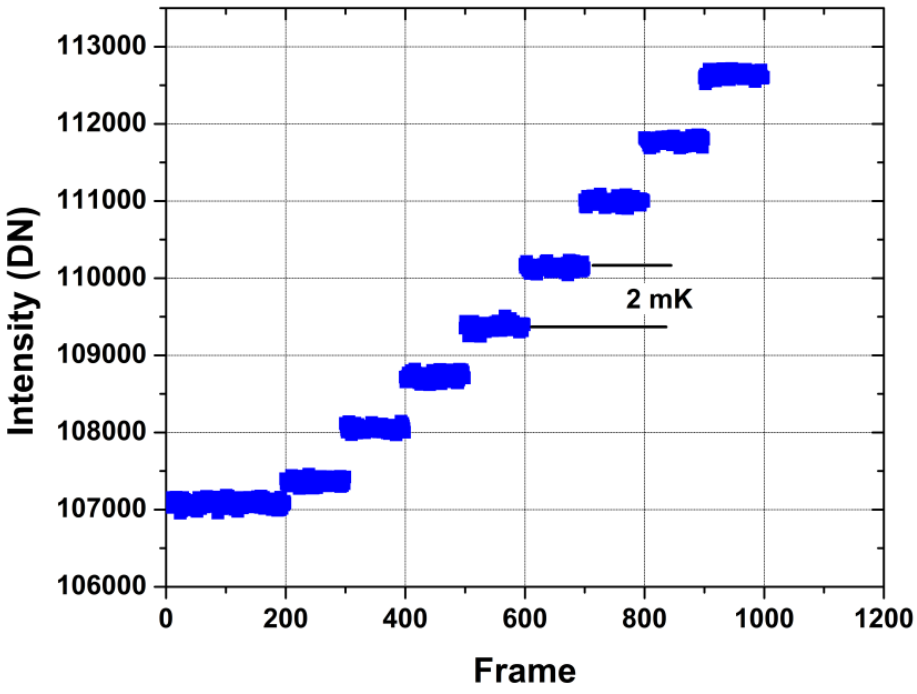

Figure 12. Signal change in digital numbers versus frame capture for 2-mK steps with the heater.

The background limited noise for this case is about 2 mK [13]. The percent change in intensity with 1-K change can range from tens of percent to hundreds of percent depending on the temperature distance from the phase transition, as was illustrated in Figure 4. In the envisioned operation of the thermal sensor, the imager will be operated near the tens of percent change per 1 K. The temperature sensitivity for the data in Figure 12 is still limited by the test system and not the LC cell. For example, the noise is that from the Poison distribution of the input light.

Other performance characteristics measured on the bulk LC cells included dynamic range and response time. The bulk LC cell is measured to have a dynamic range greater than 10 bits by stepping in 2-mK increments over 0.5 K. The temperature resolution as shown in Figure 11 is discernible across this range and relatively linear. For 225-µK steps, the maximum temperature would be 225 mK for a 10-bit dynamic range, which is well within the 3-K distance from the phase transition. It should be noted that to get a dynamic range of 10 bits, the optical imager will need to have greater than10^6 photoelectrons per pixel. The visible CMOS or CCD imager must accommodate the high signal levels [5]. Recently, imagers have been designed that have large dynamic ranges, for example, by having high charge capacity [14] or by doing an in-pixel A/D conversion [15]. We are striking a balance between sensitivity, dynamic range, and

noise. Operating too close to the phase transition causes more molecular fluctuation noise to be included in the signal.

To measure the thermal response of the LCs in bulk cells, the glass slide surface facing the LCs coated with ITO is electrically pulsed at a high frequency through the connection on one side of the cell. This heats the LC enabling the rise time of the LCs to be measured by imaging the intensity change. The rise time is measured to be less than 30 ms, which is limited by the speed of the camera system.

To learn more about the noise, the power spectral density (PSD) is measured using the Senarmont system with and without the quarter wave plate. Figure 13 shows typical PSD curves for the two conditions. A high-speed CCD camera operating at 700 Hz is used to collect the data. One important result is that the noise of the cell is dominated by the shot noise of the visible light source (Poisson distribution) for the Senarmont system with the quarter wave plate in place. Also the 1/f noise is negligible for both conditions, but instead a Lorentzian-shaped curve is seen with a flat response at low frequencies [5, 16] corresponding to LC molecule twist fluctuations. The curve starts to decrease at about 20 Hz where the roll off frequency is related to the viscosity, elastic constant, and thickness of the cell. The curve becomes constant again at high frequencies where it is dominated by the shot noise of the visible light. The quarter wave plate is important for removing most of the twist noise. Other particular arrangements can be found that reduce the twist fluctuations without the quarter wave plate, which depend on the phase retardation through the cell, the cell thickness, and alignment anchoring energy. However, the quarter wave plate removes the need for these special conditions.

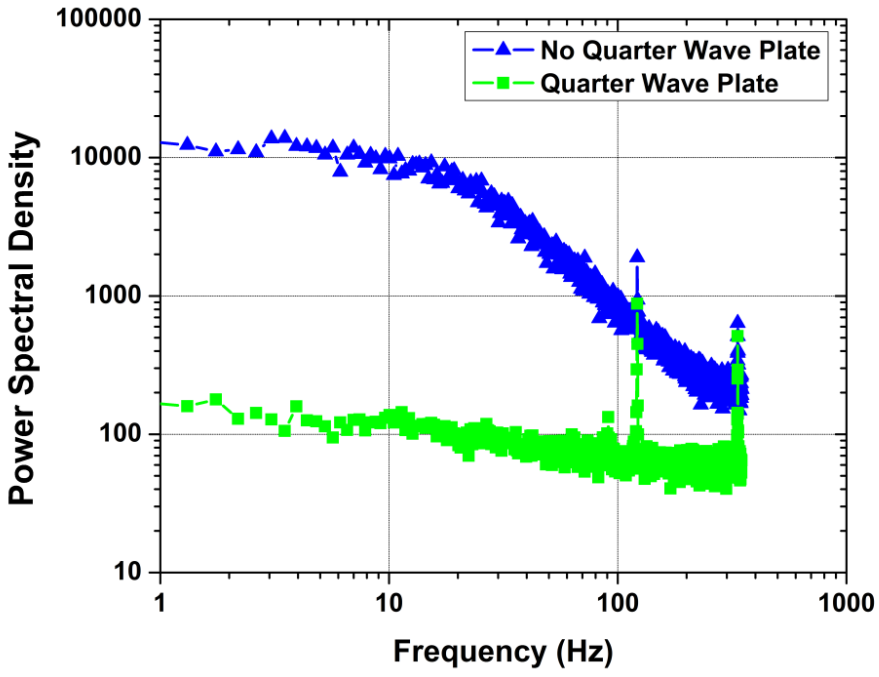

Figure 13. Power spectral density curves near the phase transition with and without the quarter wave plate.

5.2 Array Measurements

Measurements have been done on device arrays that have finished processing. The first devices are on silicon substrates (instead of fused silica) so the characterization is done in the reflection mode (instead of transmission shown in Figure 8 a). Figure 14 is a photograph of the test system. After passing through a mirror and 8- to 12-µm filter, LWIR light from a blackbody source is focused by a ZnSe lens (f/3) and then reflected by a dichroic optic into the dewar and onto the LC array. As determined through modeling, the average LWIR absorption is about 40% in the thermal pixel for the 8- to 12-µm band. A blackbody source provides the IR light, and the Senarmont method is used to detect the LC birefringence change due to the absorption of the light. The visible light source is an LED with a wavelength selected somewhere in the visible to optimize the signal and to match the quarter wave plate. The light bandwidth is reduced to about 10 nm by a filter. After going through a beam splitter, the visible light passes through a lens and is focused onto the LC array. The light reflected by the LC array is passed again through the lens and focused onto the CCD camera focal plane array.

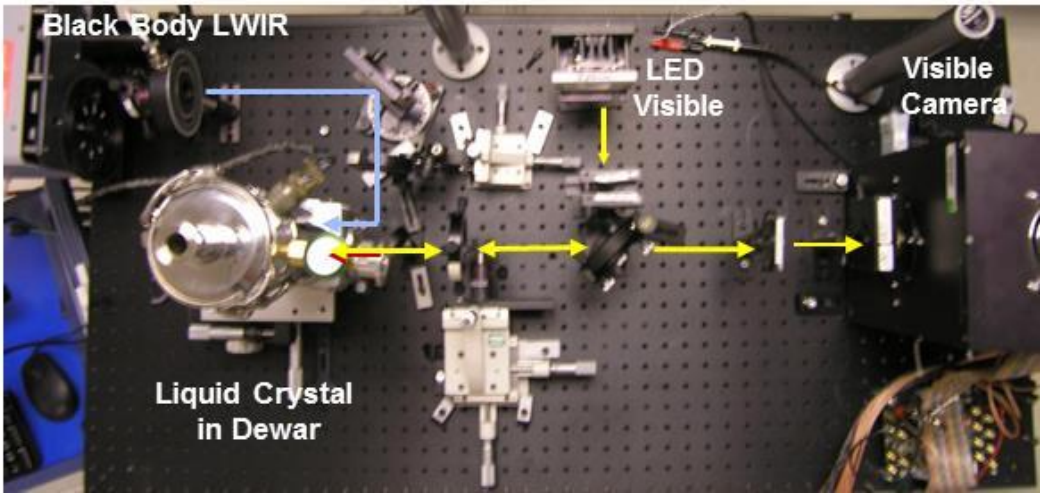

Figure 14. Photograph of the test setup with the system operating in reflection mode.

Figure 15 is a graph of the intensity versus frame capture, again using the heater to step the temperature. The sensitivity is similar to that for the bulk samples, indicating that the array processing does not significantly alter alignment properties or the temperature sensitivity. Achieving sensitivity of the LC in these small cavities is a major milestone in demonstrating that the cavity structure and alignment method does not alter our major premise for designing this array imager. The reflection-mode operation in our setup yields a response even though the conditions are very lossy and far from optimum compared to the large-area cell measurements.

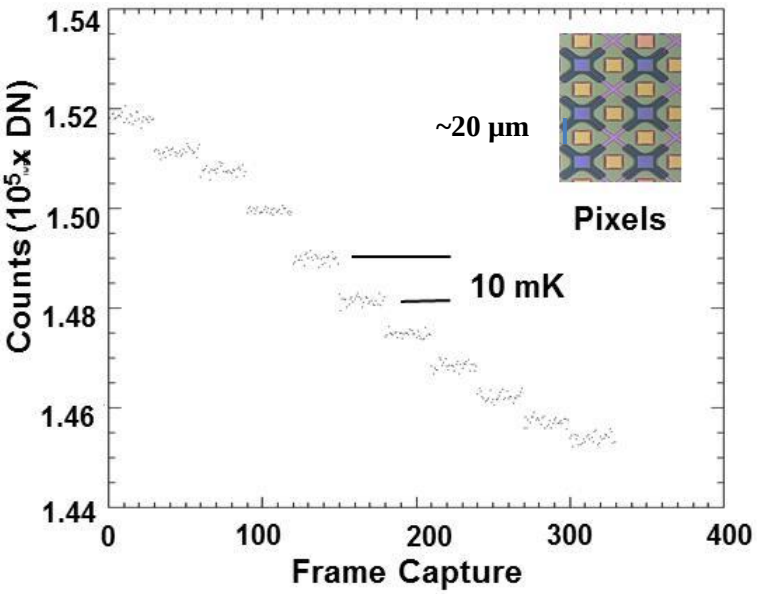

Figure 15. Signal versus frame capture using 10-mK steps. The inset shows a picture of a 2×6 array.

Figure 16 shows the response of a pixel in the array where the frames are taken at less than 1-second intervals. The camera is operating at 30 Hz but the frame grabber is capturing frames about once a second. The measured performance shows detection of temperatures in the tens of degrees centigrade range for the blackbody radiator. The present low reponse with temperature is due to several factors such as the f/3 lens, low thermal resistance (two extra silicon nitride legs), low LWIR absorption, parasitic visible light scattering, and nonoptimum operating conditions.

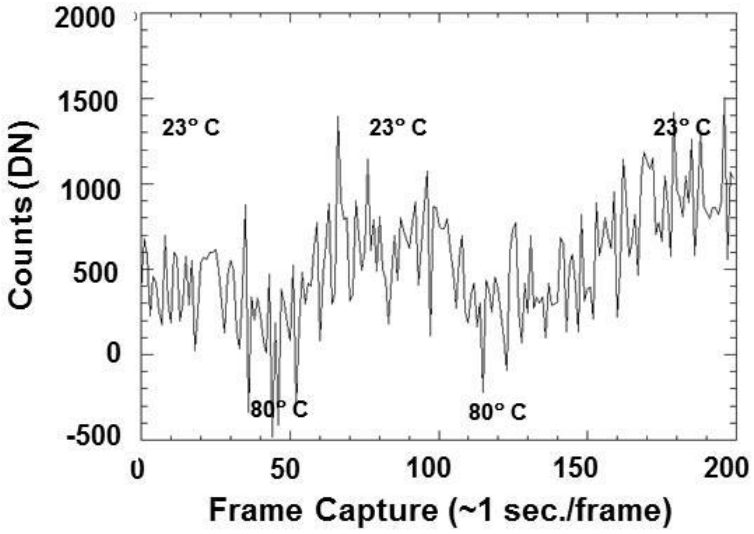

Figure 16. Pixel response from blackbody radiation source.

6.0 Summary

A technology is being developed for high-pixel-count uncooled thermal imaging arrays. The new sensor concept separates the transducer from the ROIC and has the potential to greatly simplify fabrication while having good sensitivity. The sensor uses the temperature sensitivity of the LC birefringence to build the transducer that converts the IR scene to a visible image. Preliminary results from measurements on arrays indicate that the LC material quality is similar to that of bulk samples and that good NETD performance should be possible with optimization of the pixel structure. In the future, high-fill-factor arrays on fused-silica substrates will be processed that will enable optimization of conditions for greatly improved temperature sensitivity. A better IR absorber layer will be integrated into the process and the structure will be tuned for the infrared.

7.0 Acknowledgements

This work was sponsored by the Assistant Secretary of Defense (ASD) for Research and Engineering (R&E) under Air Force Contract No. FA8721-05-C-0002. The authors would like to acknowledge Jeremy Muldavin and Steve Rabe for their contirbution on processing concepts. The authors would also like to thank Chris Caron, John Daneu, and Peter O'Brien for their help in fabricating the devices.

8.0 References

1. M. Batinica, S. Black, T. Coleman, M. Lamb, and R. Williams, "Uncooled IR Detectors for Air-To-Ground Missile Applications," Proceedings of the Military Sensing Symposia, Passive Sensors, 2012.
2. G.D. Skidmore, C. Li, C. Howard, M. Sweeney, and C.J. Han "Status of Uncooled Detectors and Camera Systems at DRS," Proceedings of the Military Sensor Symposia, Detectors, 2011.
3. R.D. Ennulat, L.E. Garin, and J.D. White, **"**The Temperature Sensitivity of the Selective Reflection by Cholesteric Mesophases and Its Possible Limitations," Molecular Crystals and Liquid Crystals, Vol. 26, Issue 3-4, pp. 245-267 (1974).
4. J.R. Hansen, J.L. Fergason, and A. Okaya, "Display of Infrared Laser Patterns by a Liquid Crystal Viewer," Applied Optics, Vol. 3, No. 8, pp. 987-988 (1964).
5. R.G. Humphreys and H.A. Tarry, "An Optically Coupled Thermal Imager," Infrared Physics, Vol. 28, No. 2, pp. 113-127 (1988).
6. P.G. deGennes and J. Prost, *The Physics of Liquid Crystals*, Second Edition, Oxford Science, 1993.
7. P. Yeh and C. Gu, *Optics of Liquid Crystal Displays*, John Wiley and Sons Inc., 1999.
8. P. Chaudhari, J. Lacey, J. Doyle, E. Galligan, S.-C. A. Lien, A Callegari, G. Hougham, N.D. Lang, P.S. Andry, R. John, K.-H. Yang, M. Lu, C. Cai, J. Speidell, S. Purushothaman, J. Ritsko, M. Samant, J. Stoehr, Y. Nakagawa, Y. Katoh, Y. Saitoh, K. Sakai, H Satoh, S. Odahara, H Nakano, J. Nakagaki, and Y. Shiota, "Atomic-Beam Alignment of Inorganic Materials for Liquid-Crystal Displays," Letters to Nature, Vol. 411, pp. 86-89 (2001).
9. D.W. Berreman, "Solid Surface Shape and the Alignment of an Adjacent Nematic Liquid Crystal," Physical Review Letters, Vol. 28, No. 26, pp. 1683-1687 (1972).
10. K. Robbie, D.J. Broer and M.J. Bret, "Chiral Nematic Order in Liquid Crystals Imposed by an Engineered Inorganic Nanostructure," Letters to Nature, Vol. 399, pp. 764-766 (1999).
11. V.G. Chigirnov, V.M. Kozenkov, and H.S. Kwok, *Photoalignment of Liquid Crystalline Materials*, John Wiley and Sons Ltd., SID Series in Display Technology, 2008.
12. *Handbook of Optics, Second Edition, Vol. 2: Devices, Measurements, and Properties*, M. Bass, Editor, McGraw Hill, Chapter 22, Polarimetry, 1995.
13. S. Horn, D. Lohrman, P. Norton, K. McCormack, and A. Hutchinson, "Reaching for the Sensitivity Limits of Uncooled and Minimally Cooled Thermal and Photon Infrared Detectors," Proceedings of SPIE, Vol. 5783, Infrared Technology and Applications XXXI, pp. 401-411, 2005.
14. M. Mori, Y. Hirose, M. Segawa, I. Miyanaga, R. Miyagawa, T. Ueda, H. Nara, H. Masuda, S. Kishimura, T. Sasaki, Yoshihisa Kato, Y. Imada, H. Asano, H. Inomata, H. Koguchi, M. Ihama, and Y. Mishima, "Thin Organic Photoconductive Film Image Sensors with Extremely High Saturation of 8500 electrons/μm^2," Symposium on VLSI Technology Digest of Technical Papers, pp. T22-T23, 2013.
15. D. Klick, M. Kelly, R. Hoffeld, C. Colonero, E. Ringdahl, J. Blanchard, D. Hearn, J. Costa, J. Baker, V. Cerrati, J. Bari, L. Retherford, and M. Huber, **"**WISP-360 Wide Area Imager using LWIR DFPA for Tower-based Persistent Surveillance," Proceedings of the Military Sensing Symposia, Passive Sensor, 2001.
16. Orsay Group, **"**Dynamics of Fluctuations in Nematic Liquid Crystals," The Journal of Chemical Physics, Vol. 51, No. 2, pp. 816-822 (1969).